Special Issue: Numerical Tools for Soils

Research Paper

Singularity maps applied to a vegetation index

CrossMark

Juan J. Martín-Sotoca [a,b], **Antonio Saa-Requejo** [a,c], **Javier Borondo** [b], **Ana M. Tarquis** [a,b,*]

[a] CEIGRAM, E.T.S.I. Agronómica, Alimentaria y de Biosistemas, Universidad Politécnica de Madrid (UPM), Spain
[b] Grupo de Sistemas Complejos, Universidad Politécnica de Madrid (UPM), Spain
[c] Dpto de Producción Agraria, E.T.S.I. Agronómica, Alimentaria y de Biosistemas, Universidad Politécnica de Madrid (UPM), Spain

ARTICLE INFO

Agricultural drought quantification is one of the most important tasks in the characterisation process of this natural hazard. Recently, several vegetation indexes based on remote-sensing data have been applied to quantify it, being the Normalized Difference Vegetation Index (NDVI) the most widely used. Some index-based drought insurances define a drought event through the comparison of actual NDVI values in a given period with a NDVI threshold based on historical data of that period extrapolating this result spatially to the surrounded areas. Hence, the spatial statistical approach is very relevant and has not been deeply studied in this context.

Drought can be highly localised, and several authors have recognised the critical role of the spatial variability. Therefore, it is important to delimit areas that will share NDVI statistical distributions and in which the same criteria can be applied to define the drought event. In order to do so, we have applied for the first time in this context the method of singularity maps commonly used in localisation of mineral deposits. The NDVI singularity maps calculated for each season and different years are shown and discussed in this context. For this study we have selected a region that includes the whole Autonomous Community of Madrid (Spain). The resulting singularity maps show that areas where the NDVI follows theoretically a spatial normal/log-normal distribution ($\alpha \cong 2$) are widely scattered in the area of study and vary across seasons and years. Therefore, the extrapolation of normal/log-normal NDVI statistics should be applied only inside these areas.

1. Introduction

1.1. Drought and vegetation indexes

Drought is one of the natural hazards with more impact on the planet and human life, becoming a natural disaster in extreme cases (Gouveia, Trigo, & DaCamara, 2009). Although there are several definitions of drought, it can generally be defined as the temporary lack of water, relative to the normal supply, for a sustained period of time (Hayes, 2004; Keyantash & Dracup, 2002).

Drought quantification is one of the most important tasks in the characterisation of this natural hazard and can be approached in different ways (Sepulcre-Canto, Horion,

---

* *Corresponding author.* CEIGRAM, E.T.S.I. Agronómica, Alimentaria y de Biosistemas, Universidad Politécnica de Madrid (UPM), Spain.
E-mail address: anamaria.tarquis@upm.es (A.M. Tarquis).

Singleton, Carrao, & Vogt, 2012). One promising way is through indexes based on remote-sensing data (Dalezios, Blanta, Spyropoulos, & Tarquis, 2014) obtained by satellites or drones. These aircraft have spectro radiometric sensors installed on board (AVHRR, MODIS, among others) which are able to detect different frequency bands to obtain surface-Earth images at periodic time intervals. The combination of these frequency bands derives to Vegetation Indexes (VI). These indexes show the Photosynthetically Active Radiation (PAR) absorption of green leaves. The VI are associated with fundamental hydro-ecological processes such as precipitation, which in turn is also directly linked to photosynthesis and hence plant growth. The most widely used VI are: Normalized Difference Vegetation Index (NDVI), Soil Adjusted Vegetation Index (SAVI) and Enhanced Vegetation Index (EVI).

1.2. Statistical approaches in VI spatial variability

It is important to note that more and more index-based agricultural insurances are defining a drought event through the comparison of the current VI value in a given period with a VI threshold based on historical data (Chantarat, Mude, Barrett, & Carter, 2013; Makaudze & Miranda, 2010). In this scenario, the statistical assumptions made to calculate this threshold will be crucial since different statistical approaches will lead to different conclusions.

The VI maps usually present a high variability in their values (Scheuring & Riedi, 1994). In the most common approach, the spatial variable under study is considered to be a random process and the main indicator measuring the spatial variability is the semivariogram, a second-order statistical moment of the spatial variable (Peebles, 1987). The most usual assumption is the "intrinsic hypothesis" where the semivariogram only depends on the lag distance (stationary process) and all the regionalised variables are considered Gaussian (Journel & Huijbregts, 1978).

There is an alternative approach to measure the spatial variability in singular physical processes by Multifractal Analysis (MFA). Singular processes are normally non-linear systems whose final results can be modelled by fractals or multifractals (Evertsz & Mandelbrot, 1992; Feder, 1989; Schertzer & Lovejoy, 1991). Fractality and multifractality (scaling laws) are emergent general features of ecological and geological systems (Saravia, Giorgi, & Momo, 2012; Turcotte, 1997), and they reflect constraints in their organisation that can provide tracks about the underlying mechanisms (Solé & Bascompte, 2006). Some examples of singular processes in the context of natural systems are: cloud formation (Schertzer & Lovejoy, 1987), rainfall (Veneziano, 2002), hurricanes (Sornette, 2004), etc. MFA should be used when a spatial distribution shows a singular character and extreme values (anomalies) are relevant (Cheng, 1999a). Outcomes of such singular processes are often described by positively-skewed distributions with Pareto upper-value tails (Agterberg, 1995; Cheng, Agterberg, & Ballantyne, 1994; Lavallee, Lovejoy, Schertzer, & Ladoy, 1993).

1.3. The singularity index

In the context of MFA, we can characterise the anomalous spatial behaviour of singular processes by the singularity index or exponent. The mapping of singularity exponents in multifractal measures has proved to be a very effective tool in delineating areas with anomalies in measure distributions. Cheng (1999a, 2008) elaborated a local singularity analysis based on multifractal modelling that provides a powerful tool for characterising the local structural properties of spatial patterns. Taking the notation of MFA, the behaviour around a location x of a multifractal measure μ can be described as a power-law relationship:

$$\mu(B(x,r)) \sim r^{\alpha(x)}, \tag{1}$$

where $B(x,r)$ is a set centred at x with radius $r \rightarrow 0$. The exponent of this power-law model is the singularity exponent $\alpha(x)$ and characterises the degree of anomalous behaviour. The singularity exponent usually has finite values around the support topological dimension (E) and varies within a finite range from α_{min} to α_{max}. Singularity map is defined as the locus of the points x that have the same singularity exponent (Falconer, 2003), calculated by the expression:

$$\alpha(x) = \lim_{r \rightarrow 0} \frac{\ln \mu(B(x,r))}{\ln r}, \tag{2}$$

This tool has been successfully applied to detect anomalies in the concentration of an element (Cheng, 2001, 2006, 2007; Xie, Cheng, Chen, Chen, & Bao, 2007), which helps to delimit potential deposits (Cheng, 1999a). In the case of anomaly detection in element concentration maps, Cheng (2001) stated that the mean element concentration Z(x), calculated for various cell sizes r centred at x, obeys a power-law with r:

$$Z(x) \sim r^{\alpha(x)-E}, \tag{3}$$

where $E = 2$ in this type of maps. This power-law is fulfilled in a certain range of r, $[r_{min}, r_{max}]$, obtaining a singularity map.

In the above work, points with $\alpha(x) \cong 2$ (where $\cong$ means "approximately equal to") are named as "non-singular locations" and represent areas with constant mean element concentrations. Points with $\alpha(x) \neq 2$ are named as "singular locations", and we can differentiate areas with positive singularities ($\alpha(x) < 2$) corresponding to anomalously high values of mean concentration in a geochemical map, and negative singularities ($\alpha(x) > 2$) corresponding to low mean concentration values. Then, the Concentration–Area (CA) method was applied to calculate the threshold of positive and negative singularities (Liu, Xia, Cheng, & Wang, 2013). Therefore, calculating the singularity map for a geochemical concentration map may be used to characterise concentration patterns which provide useful information for interpreting anomalies related to local mineralisation processes.

Another useful interpretation of the singularity exponent is related to geostatistics (Cheng, 2008). This interpretation states that the majority of locations on the map where $\alpha(x) \cong 2$ (non-singular locations) follows either normal or lognormal distributions, whereas the singular locations (positive and negative singularities) on the map with $\alpha(x) \neq 2$ may follow extreme value Pareto distributions. The majority of common statistical techniques which require the assumption of normal distributions and the intrinsic hypothesis may not be effective for studying data with extreme value distributions, as happens in multifractal processes.

1.4.　Objectives

In this work, NDVI is the spatial distribution under study. NDVI maps have a multifractal character (Alonso, Tarquis, & Benito, 2005; Alonso, Tarquis, Benito, & Zúñiga, 2007, 2008; Lovejoy, Tarquis, Gaonac'h, & Schertzer, 2008; Poveda & Salazar, 2004) representing an underlying singular process. The aim of this work is to check if that multifractal character holds, to estimate singularity maps of NDVI images and to extrapolate the conclusions obtained by Cheng for chemical element concentration maps and Pareto statistics. This study will also explore if singularity maps could be applied to delineate areas with anomalies in the NDVI concentration at different times in the year. Finally, we are mainly interested in places where singularity exponents satisfy $\alpha(x) \cong 2$, (non-singular locations) since these places will follow normal or lognormal distributions in NDVI values, and so we can apply a normal statistical assumption over these areas, very useful in index-based agricultural insurances.

This is the first time that this well-known methodology in the multifractal field is applied to NDVI maps. For this purpose a region that includes the Autonomous Community of Madrid in Spain will be studied at each season for two different years (dry and wet one).

2.　Materials and methods

2.1.　Normalized Difference Vegetation Index (NDVI)

NDVI shows vegetation photosynthetic activity (Flynn, 2006). Photosynthetic activity is related to the moisture that crops need to grow properly, the greater the moisture availability, the higher photosynthetic activity. The latter is not a completely accepted statement by all experts pointing out that NDVI essentially relates to the effective proportion of the image region that is green leaf tissue, and so NDVI has no direct link to photosynthetic activity, but to photosynthetic capacity. In any case, it is reasonable to study drought through NDVI, except for physiological drought cases. There are other more accurate indices that incorporate soil effects and atmospheric influences, however for simplicity and ease of interpretation we will use NDVI in this paper. To calculate NDVI we will use this mathematical formula:

$$NDVI = \frac{IRc - R}{IRc + R} \tag{4}$$

where IRc and R are the reflectance values in the Near-Infrared band and Red band respectively. The range of NDVI values is from -1 to $+1$. Values below zero indicate no photosynthetic activity and are characteristic of areas with large accumulation of water such as rivers, lakes, reservoirs, etc. The higher is the NDVI value, the greater is the photosynthetic activity.

2.2.　Study area

For the spatial study we consider a rectangular region that includes the whole Autonomous Community of Madrid (ACM), Spain. This area consists of 300×280 pixels each one representing an area of 500 m $\times$ 500 m (see Fig. 1).
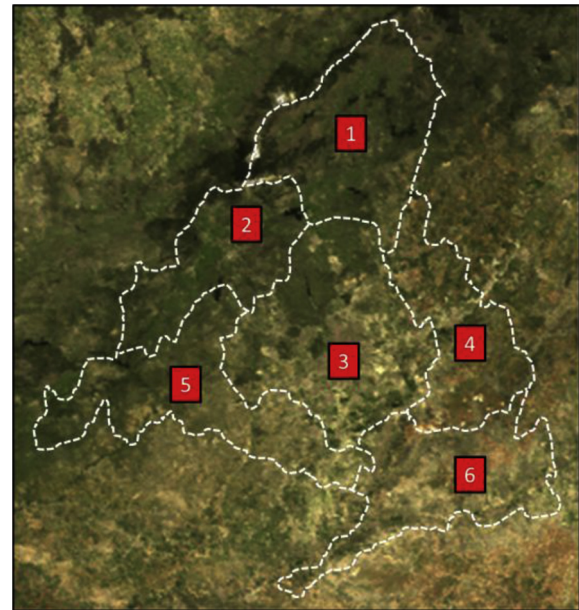

Fig. 1 – **RGB image of the rectangular area with 300 × 280 pixels used for spatial study (MODIS capture date: 15/04/2011). The dashed line gives the contours of the Autonomous Community of Madrid and the six agricultural regions: (1) Lozoya-Somosierra, (2) Guadarrama, (3) Metropolitan area, (4) Campiňa, (5) South-West and (6) Las Vegas.**

UTM30 coordinates of the boundaries corresponding to pixels centre of this area are:

(1) Top left corner: 360162 m E, 4560040 m N.
(2) Top right corner: 499662 m E, 4560040 m N.
(3) Bottom left corner: 360162 m E, 4410540 m N.
(4) Bottom right corner: 499662 m E, 4410540 m N.

This rectangle represents an extension of 150 × 140 km involving two major units: the mountains and the plain of the Tagus river, separated by the foothills. The altitude range between 430 m in the final stretch of the Alberche river in the south-east and 2428 m at the peak of Peñalara in the north.

Despite its small area, ACM presents two distinct climates, as a result of its location between the Central System and the Tagus Valley. The highest areas of the Guadarrama and Ayllón in the north, above an altitude of 1200 m, have mountain climate. This implies cold or very cold temperatures in winter and mild in summer. Here, precipitation is abundant and could be greater than 1500 mm year^{-1}, in the form of snow during the winter and part of the spring and autumn (Sotelo Pérez, 2013).

The rest of ACM has a continental Mediterranean climate with warm summers. These are attenuated in the piedmont and extreme in the plateau plain. In these areas the winters are cool, with temperatures below 8 °C, very frequent night frost and occasional snowfall. By contrast, summers are hot, with average temperatures above 24 °C in July and August and with maximums often exceeding 35 °C. Rainfall does not usually exceed 700 mm year^{-1} and is concentrated especially in the spring and autumn (Sotelo Pérez, 2013).

2.3. Remote sensing database

Information provided by the scientific research satellite Terra (EOS AM-1) has been chosen to calculate NDVI in the study area. This satellite was launched into orbit by NASA on December 18th 1999. The MODIS (Moderate Resolution Imaging Spectroradiometer) sensor provides information by frequency bands.

MODIS information is organised by "products". The product we have used is MOD09A1 (LP DAAC, 2014), which incorporates seven frequency bands: Band 1 (620–670 nm), band 2 (841–876 nm), band 3 (459–479 nm), band 4 (545–565 nm), 5 band (1230–1250 nm), band 6 (1628–1652 nm) and band 7 (2105–2155 nm). The bands used to calculate NDVI are: band 1 for red frequency and band 2 for near-infrared frequency. MOD09A1 provides geo-referenced images with pixel resolution of 500 m × 500 m. This product has a mix of the best reflectance measures of each pixel in an 8-day period. Used format file is GeoTIFF with geo-referenced UTM30 information and geode model WGS 84.

For spatial analysis we compare the results obtained on four different dates over two 1-year periods, 2005 (dry year) and 2011 (wet year). We have taken approximately the same representative date for each season. Selected dates are:

- (Winter): 17th of January 2005 and 25th of January 2011.
- (Spring): 23th of April 2005 and 15th of April 2011.
- (Summer): 20th of July 2005 and 20th of July 2011.
- (Autumn): 24th of October 2005 and 24th of October 2011.

2.4. Multifractal analysis

The aim of a multifractal analysis (MFA) is to study how a normalised probability distribution or a measure $\mu(x)$ varies with scale r. Let us consider a grid of cells of size r covering a measure $\mu(x)$ on $\mathbb{R}$, with total length size L. The measure of the cell i of size r is $M_i(r)$ and can be calculated by the following expression:

$$M_i(r) = \int_{x_i}^{x_i+r} \mu(x)dx \tag{5}$$

Then, the normalised probability distribution of the cell i of size r is defined as:

$$\mu_i(r) = \frac{M_i(r)}{\sum_{j=1}^{N(r)} M_j(r)}, \tag{6}$$

where $N(r)$ is the number of cells of size r included on total length L. For a multifractal measure, the partition function $\chi(q,r)$ has scaling properties (Evertsz & Mandelbrot, 1992), namely,

$$\chi(q,r) = \sum_{j=1}^{N(r)} \mu_j^q(r) \sim r^{\tau(q)}, \tag{7}$$

where $\tau(q)$ is a nonlinear function of q called the "mass exponent function" (Feder, 1989). For each q, $\tau(q)$ may be obtained as the slope of a log–log plot of $\chi(q,r)$ vs. r. This method

is known as the "method of moments" (Halsey, Jensen, Kadanoff, Procaccia, & Shraiman, 1986).

The singularity exponents α can be determined by the Legendre transformation of the $\tau(q)$ curve as:

$$\alpha(q) = \frac{d\tau(q)}{dq} \tag{8}$$

The number of cells of size r with the same singularity exponent α, $N_\alpha(r)$, is related to the cell size as,

$$N_\alpha(r) \propto r^{-f(\alpha)} \tag{9}$$

Therefore, $f(\alpha)$ is a scaling exponent which is the fractal dimension of the set $N_\alpha(r)$. Parameter $f(\alpha)$ can be calculated as:

$$f(\alpha) = q\alpha(q) - \tau(q) \tag{10}$$

Properties of the functions $\alpha(q)$, $\tau(q)$ and $f(\alpha)$ have been discussed by several authors (e.g. Cheng & Agterberg, 1996; Feder, 1989; Schertzer & Lovejoy, 1991).

The multifractal spectrum (MFS), i.e., a graph of α vs. $f(\alpha)$, quantitatively characterises variability of the measure studied with asymmetry to the right and left indicating scaling domination of small and large values respectively. The width of the MFS indicates overall variability (Tarquis, Losada, Benito, & Borondo, 2001).

2.5. The Concentration–Area (C–A) method

When a variable $Z(x,y)$ follows a fractal/multifractal model, the C–A method (Cheng et al., 1994) establishes power-law relationships between the values z of the spatial-dependent variable $Z(x,y)$ and the area A enclosed by these values:

$$A(Z(x,y) \geq z) \propto z^\beta, \tag{11}$$

where A is the area constituted by values greater than a given value z and β is the characteristic exponent of the C–A method. These power-law relationships are converted to linear segments in a log–log plot. The C–A method uses the slope-changed points to calculate thresholds in the variable $Z(x,y)$ which define different sets.

The spatial variability of the singularity exponents $\alpha(x,y)$ also satisfies a fractal/multifractal model. Then, linear segments can be determined from the singularity-area relationship:

$$A(\alpha(x,y) \geq c) \propto c^\beta, \tag{12}$$

where A is the area constituted by singularity exponents $\alpha(x,y)$ greater than a given value c and β is the characteristic exponent of the C–A method (Liu et al., 2013). In the context of two dimensional maps, the slope-change point in the log–log plot is used to establish the threshold α_{Tmin} in the theoretical set of positive singularities ($\alpha(x,y) < 2$). Therefore, the real set of positive singularities is defined by the expression:

$$\alpha(x,y) < \alpha_{Tmin} < 2 \tag{13}$$

In the same way, a threshold α_{Tmax} can also be calculated in the set of negative singularities ($\alpha(x,y) > 2$) using the following expression:

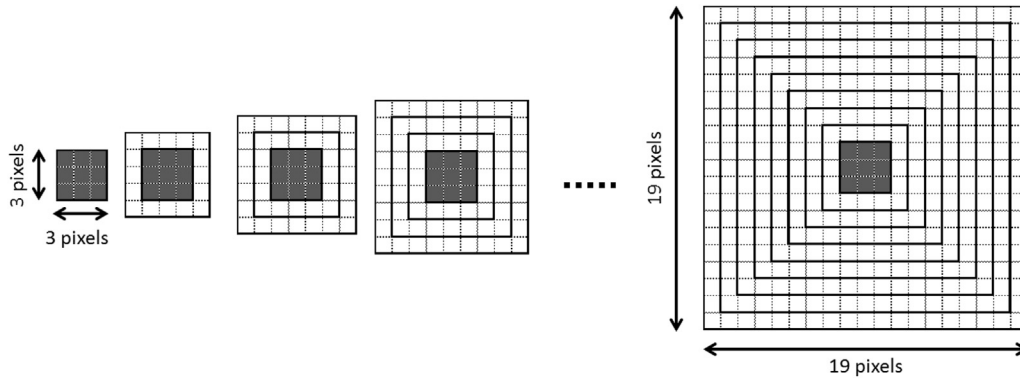$$A(\alpha(x,y) \leq c) \propto c^\gamma \tag{14}$$

Fig. 2 − Square window of variable side, from $r_{min} = 3$ pixels to $r_{max} = 19$ pixels, used to calculate the singularity exponent at each location (pixel). Nine window sizes derive to nine values to calculate the slope $\alpha(x)$ in a log−log plot.

where A is the area constituted by singularity exponents $\alpha(x,y)$ lower than a given value c and β is the characteristic exponent of the C−A method. Therefore, the real set of negative singularities is defined by the expression:

$$\alpha(x, y) > \alpha_{Tmax} > 2. \tag{15}$$

Using both thresholds, the set of non-singular locations ($\alpha(x) \cong 2$) is defined by the expression:

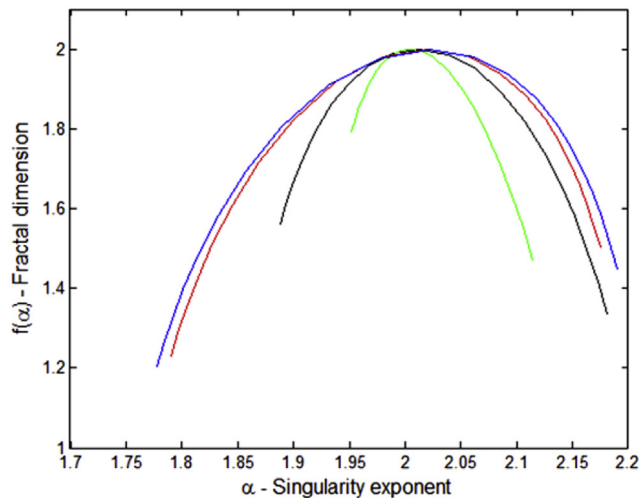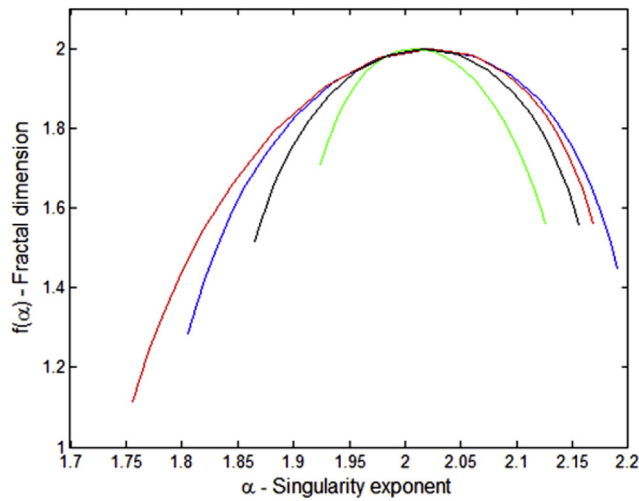$$\alpha_{Tmin} \leq \alpha(x) \leq \alpha_{Tmax} \tag{16}$$

3.   Results and discussion

For the multifractal and singularity analysis, the initial images of 300 × 280 pixels containing the ACM (Spain) were cut and centred to obtain images of 256 × 256 pixels. This was necessary to correctly apply the method of moments used to calculate the MFS. NDVI values were calculated for each pixel and the spatial distribution of the NDVI map was considered as a measure or mass distribution μ on $\mathbb{R}^2$. To ensure the validity of the multifractal calculation, all negative NDVI values were converted to zero following other works (Alonso, Tarquis, Zúñiga, & Benito, 2017).

Let $A(a_{j,k})$ be the matrix of 256 rows × 256 columns with NDVI values. First, the matrix is normalised, so that the probability value of the i-th cell of side r is:

$$\mu_i = \frac{\sum_{j,k \in i-cell} a_{j,k}}{\sum\limits_{j=1}^{256} \sum\limits_{k=1}^{256} a_{j,k}} \tag{17}$$

Fig. 3 − (Top) Multifractal spectrums for the 2005-year NDVI maps: 17/01/2005 (black), 23/04/2005 (green), 20/07/2005 (red) and 24/10/2005 (blue). (Bottom) Multifractal spectrums for the 2011-year NDVI maps: 25/01/2011 (black), 15/04/2011 (green), 20/07/2011 (red) and 24/10/2011 (blue).

Table 1 − Extreme singularity exponents ($\alpha_{max}, \alpha_{min}$), the difference ($\Delta\alpha = \alpha_{max} - \alpha_{min}$), extreme fractal dimensions ($f(\alpha_{max}), f(\alpha_{min})$) and the difference ($\Delta f = f(\alpha_{max}) - f(\alpha_{min})$) for all the analysed dates and years (2005 and 2011).

	α_{min}	α_{max}	$\Delta\alpha$	$f(\alpha_{min})$	$f(\alpha_{max})$	Δf
2005						
Winter (17/01/2005)	1.87	2.16	**0.29**	1.52	1.56	**0.04**
Spring (23/04/2005)	1.92	2.13	**0.21**	1.71	1.56	**−0.15**
Summer (20/07/2005)	1.76	2.17	**0.41**	1.12	1.56	**0.44**
Autumn (24/10/2005)	1.81	2.19	**0.38**	1.29	1.45	**0.16**
2011						
Winter (25/01/2011)	1.89	2.18	**0.29**	1.56	1.34	**−0.22**
Spring (15/04/2011)	1.95	2.11	**0.16**	1.79	1.47	**−0.32**
Summer (20/07/2011)	1.79	2.18	**0.39**	1.23	1.50	**0.27**
Autumn (24/10/2011)	1.78	2.19	**0.41**	1.20	1.45	**0.25**

Bold columns refer to the parameters used for the Multifracral Spectrum.comparison.
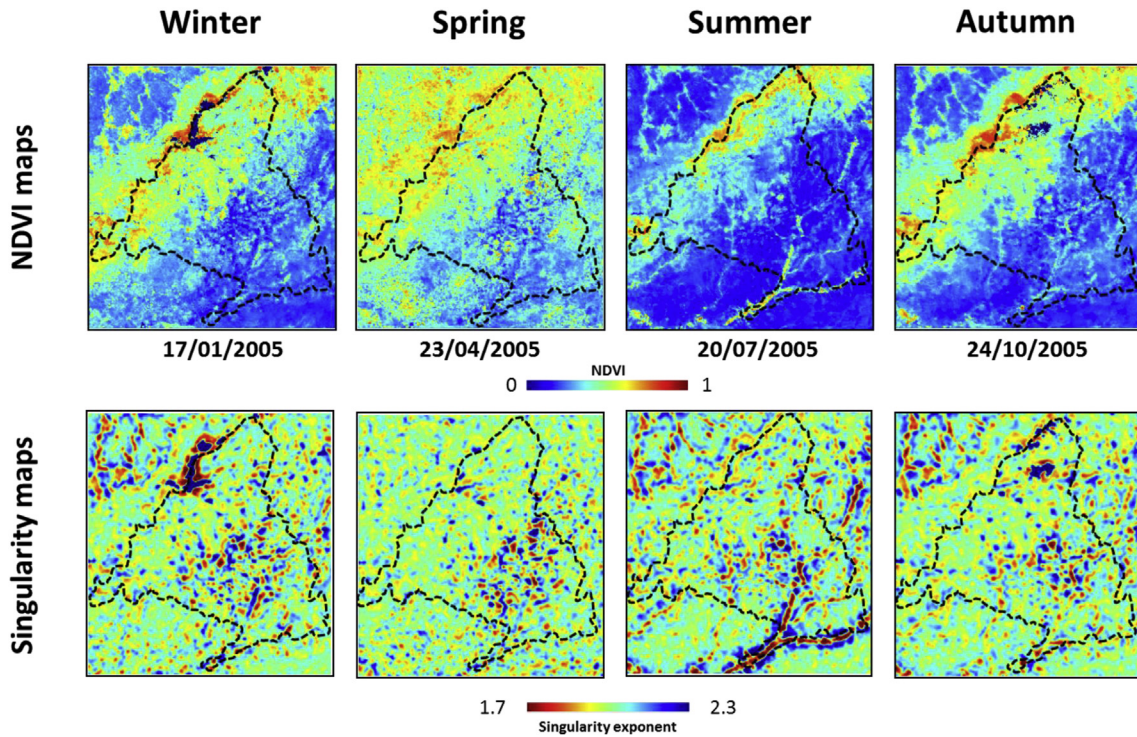
Fig. 4 – **(Top)** NDVI maps (247 × 247 pixels), and **(bottom)** singularity maps (247 × 247 pixels) for each analysed date in year 2005. Dashed lines are the limits of the Autonomous Community of Madrid. In NDVI maps, dark blue represents $NDVI_{min} = 0$ and dark red represents $NDVI_{max} = 1$. In singularity maps, the colour-map is transposed, i.e., the reddish colours indicate positive singularities (singularity exponents $\alpha < 2$) and the bluish colours indicate negative singularities (singularity exponents $\alpha > 2$). For better visualisation, singularity values less than 1.7 were collapsed to 1.7, and singularity values greater than 2.3 were collapsed to 2.3, to highlight positive and negative singularities
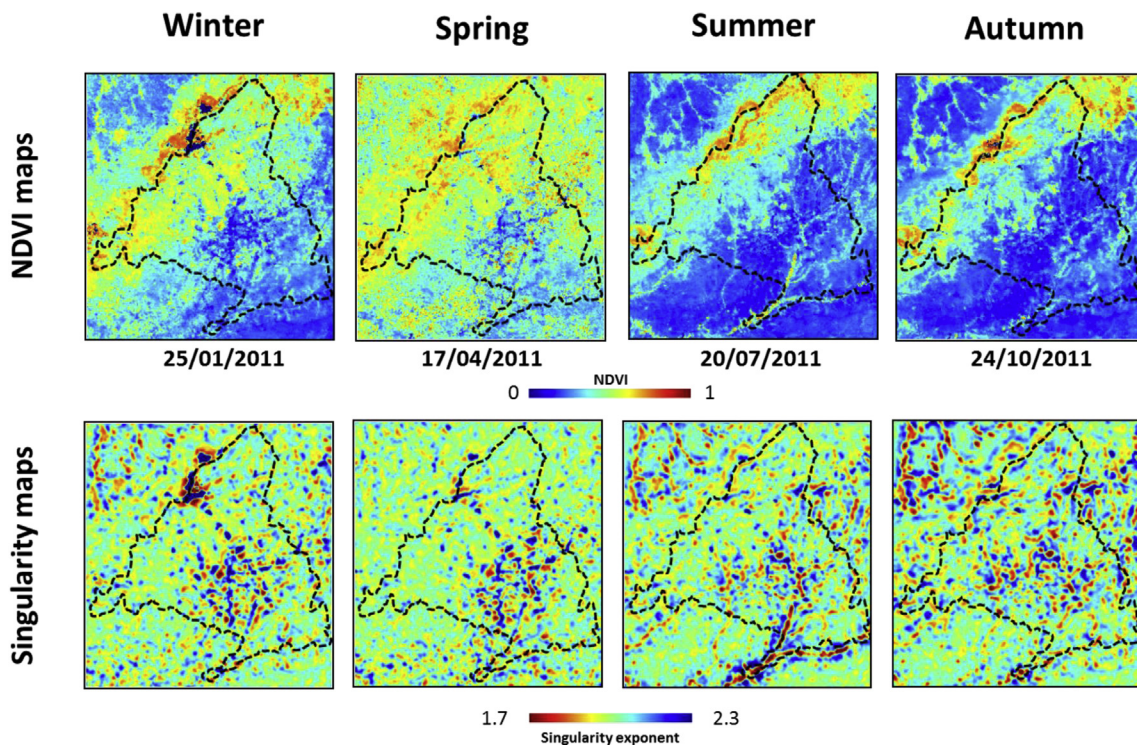

Fig. 5 – **(Top)** NDVI maps (247 × 247 pixels), and **(bottom)** singularity maps (247 × 247 pixels) for each analysed date in year 2011. Dashed lines are the limits of the Autonomous Community of Madrid. Colours as in Fig. 4.
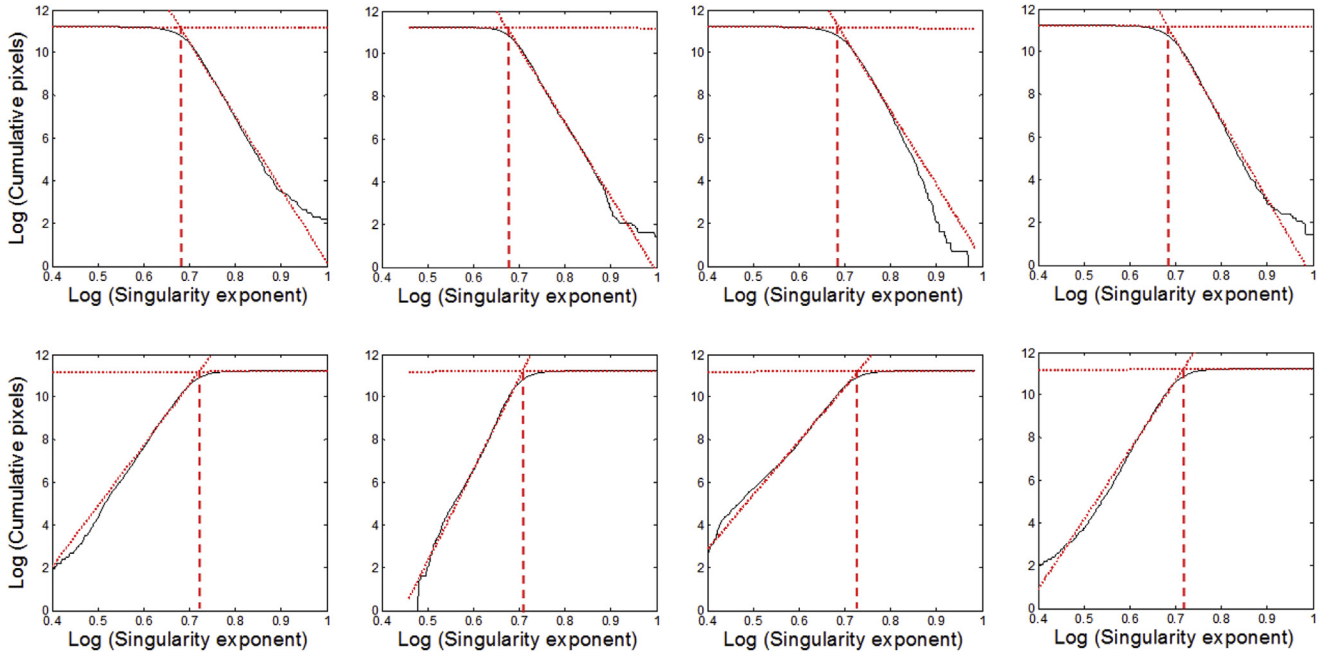
Fig. 6 – C–A method application. Log–log cumulative distributions with two regression lines (red dotted lines) for obtaining α_{Tmin} and α_{Tmax} thresholds. (Top – from left to right) The lower thresholds: α_{Tmin}(17/01/05) = 1.973, α_{Tmin}(23/04/05) = 1.961, α_{Tmin}(20/07/05) = 1.988, and α_{Tmin}(24/10/05) = 1.979. (Bottom – from left to right) The upper thresholds: α_{Tmax}(17/01/05) = 2.057, α_{Tmax}(23/04/05) = 2.028, α_{Tmax}(20/07/05) = 2.074, and α_{Tmax}(24/10/05) = 2.047. (For interpretation of the references to colour in this figure legend, the reader is referred to the web version of this article.)

All the MFS and singularity maps were performed in MATLAB. For the singularity map calculation, the windows-based method was used (Cheng, 2001) to obtain the singularity exponents of the NDVI map, i.e., the expression (2) was applied using a sliding window (a square window) of variable sides $r_{min} = r_1 < r_2 < \ldots < r_n = r_{max}$. The sides used in the analysed NDVI maps were $r_{min} = 3\,pixels$ and $r_{max} = 19\ pixels$ (see Fig. 2). Hence, nine values were used to calculate the slope
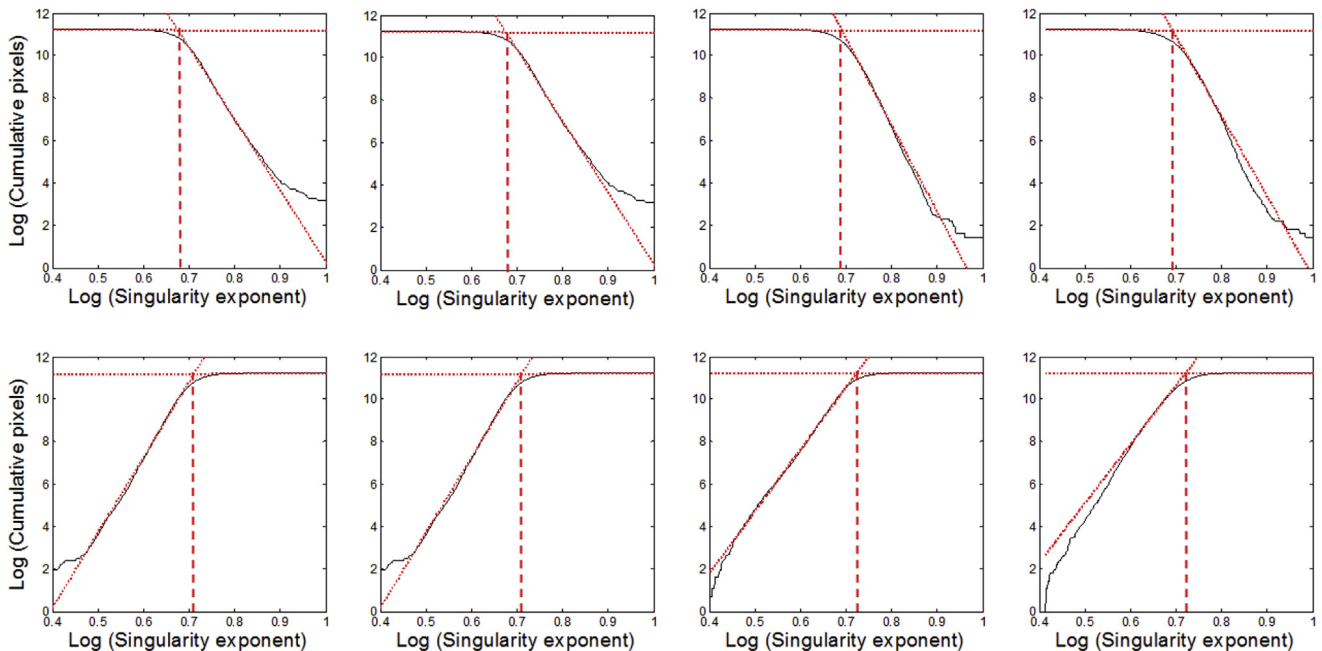

Fig. 7 – C–A method application. Log–log cumulative distributions with two regression lines (red dotted lines) for obtaining α_{Tmin} and α_{Tmax} thresholds. (Top – from left to right) The lower thresholds: α_{Tmin}(25/01/11)=1.965, α_{Tmin}(15/04/11)=1.953, α_{Tmin}(20/07/11)=1.997, and α_{Tmin}(24/10/11)=1.999. (Bottom – from left to right) The upper thresholds: α_{Tmax}(25/01/11)=2.036, α_{Tmax}(15/04/11)=2.029, α_{Tmax}(20/07/11)=2.059, and α_{Tmax}(24/10/11)=2.055. (For interpretation of the references to colour in this figure legend, the reader is referred to the web version of this article.)
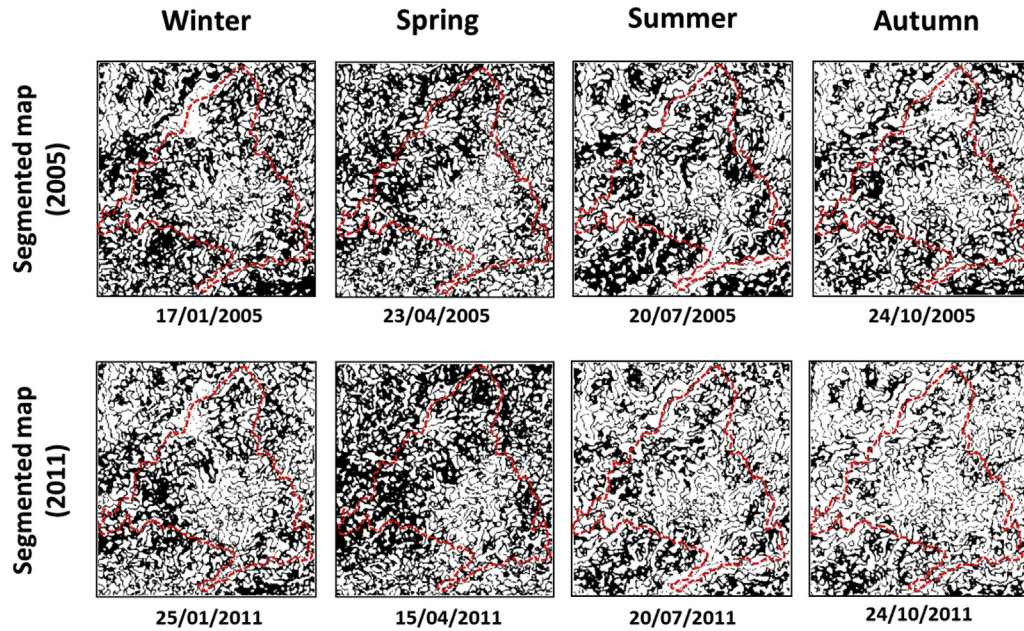
Fig. 8 – Non-singular areas shown as black pixels, where $\alpha_{Tmin} \leq \alpha(x) \leq \alpha_{Tmax}$, for all analysed dates and years. Dashed lines are the limits of the Autonomous Community of Madrid.

$\alpha(x)$ by the least-square linear regression method obtaining an $R^2 > 0.99$ in all the locations.

3.1. Multifractal analysis

An MFA was applied to all NDVI maps previously detailed (four different dates over two 1-year periods). In all cases, a linear relationship was found between the log–log plot of the partition function $\chi(q,r)$ vs. the scale (r) for a range from 2^2 pixels side-square (2 km side-square) to 2^8 pixels side-square (128 km side-square) obtaining R^2 higher than 0.98. From the slope estimated for each q, a nonlinear mass exponent function $\tau(q)$ was obtained reflecting a scaling hierarchical structure, typical of multifractal measures. The result $\tau(q = 1) = 0$ shows the conservative character of the measure. The MFS was estimated in an interval of $q = \pm 10$ with increments of 1 (Fig. 3).

All the MFS are convex parabolic curves (Fig. 3) with a variable symmetry depending on the studied NDVI season-dependent maps. In a fractal system, the MFS is shown as a single point; therefore, these results support the hypothesis of a multifractal behaviour, rather than fractal, of NDVI maps in

agreement with previous works (Alonso et al., 2017; Lovejoy et al., 2008).

MFS show important differences in amplitudes and symmetries. These concepts can be quantified by the difference of the extreme singularities ($\Delta\alpha = \alpha_{max} - \alpha_{min}$) and the difference of their respective $f(\alpha)$ values ($\Delta f = f(\alpha_{max}) - f(\alpha_{min})$). In this way, the wider is $\Delta\alpha$, the higher is the complexity of the structure studied in the NDVI map; and the wider is Δf, the higher is the asymmetry presented in the MFS. To follow other works that use these concepts, we will define right handed if $\Delta f < 0$ and left handed if $\Delta f > 0$ (Alonso et al., 2017). In Table 1, all these values are shown for all the analysed seasons and years.

Studying the evolution of $\Delta\alpha$ through a year, we realise that $\Delta\alpha$ yields the smallest value during spring, increasing in summer and autumn, reaching the maximum value during the latter season, and then decreasing in winter. This behaviour is similar in both years (2005 and 2011), so it is general cyclic behaviour, independent of whether the year is dry or wet. The meaning of $\Delta\alpha$, increasing its value through the seasons, is that the NDVI maps show a higher hierarchical spatial structure among scales showing a maximum at autumn, a season when rainfall begins and temperatures decrease mainly at the north of ACM.

With respect to the evolution of Δf through a year, the symmetry changes from right handed, in winter and spring, to left handed, in summer and autumn. This means that lower NDVI values are driving the scaling behaviour in winter/spring as such part of the MFS corresponds to calculations using negative q values. By contrast, the higher NDVI values are driving the scaling behaviour in summer/autumn as MFS left hand corresponds to positive q values. The maximum right handed asymmetry is achieved in spring, a season with rainfall mainly in the north of ACM and temperature increasing rapidly in the south. The maximum left handed

Table 2 – The upper rows "Year 2005 (dry)" and "Year 2011 (wet)" show: % of non-singular areas respect to the total area for all the analysed dates (seasons). The bottom row shows: % of non-singular intersection area respect to the total area for all the analysed dates (seasons).

	Winter	Spring	Summer	Autumn
Year 2005 (dry)	41.6%	39.9%	39.7%	34.5%
Year 2011 (wet)	36.6%	46.3%	31.4%	25.6%
Intersection	24.4%	27.2%	24.3%	14.7%

asymmetry is achieved in summer, the driest season in ACM in which higher NDVI values are reflecting areas with higher soil moisture. The evolution of Δf through a year is independent of whether the year is dry or wet. However, comparing the dry year (2005) to the wet year (2011), Δf asymmetry increases in winter/spring of the wet year. By contrast, Δf asymmetry decreases in summer of the wet year. In autumn it is very difficult to establish a pattern due to its high variability, but it is reasonable to think that it has a similar behaviour to summer.

Therefore, the cyclic evolution of $\Delta \alpha$ and Δf is describing the variation in complexity and in the importance of high or low NDVI values through the seasons. Summer and autumn show higher complexity and the scaling behaviour is dominated by the highest NDVI values. On the other hand, winter and spring have lower complexity and the lowest NDVI values are dominating the scaling behaviour. By the MFA, the NDVI spatial pattern and their scaling properties through the seasons are clearly revealed.

3.2. Singularity maps and C–A method

Two rows of images are shown in Figs. 4 and 5: the NDVI maps and the singularity maps for the analysed dates (Fig. 4 for 2005 dates and Fig. 5 for 2011 dates). A "jet" colour-map was used for better visualisation.

The maximum size of the sliding window (19 × 19 pixels) causes an edge effect on the 256 × 256 images, so that it is unable to calculate the singularities in a frame 9 pixels wide. This is the reason that singularity maps have a size of (256–9) × (256–9) pixels (247 × 247 pixels).

Areas of positive and negative singularities appear on the singularity maps obtained. It is visually appreciated that positive singularities ($\alpha < 2$) represented by reddish colours are highly correlated with riverbanks in the dry season (summer) and negative singularities ($\alpha > 2$) represented by bluish colours appear mostly on the city of Madrid and outlying cities.

The thresholds to delimit the non-singular areas, α_{Tmin} and α_{Tmax}, were calculated by the C–A method. The C–A method provided the upper and lower thresholds ($\alpha_{Tmin}, \alpha_{Tmax}$) for each of the dates analysed. In Fig. 6 (for year 2005) and Fig. 7 (for year 2011), log–log graphs are shown with slope-change points which define the sought thresholds. In all cumulative log–log graphs it was possible to calculate the slope-change points due to the existence of two linear segments. The least-square linear regression method was used to obtain the equations of both lines and to calculate the crossing point or slope-change point. The selection of points used for the
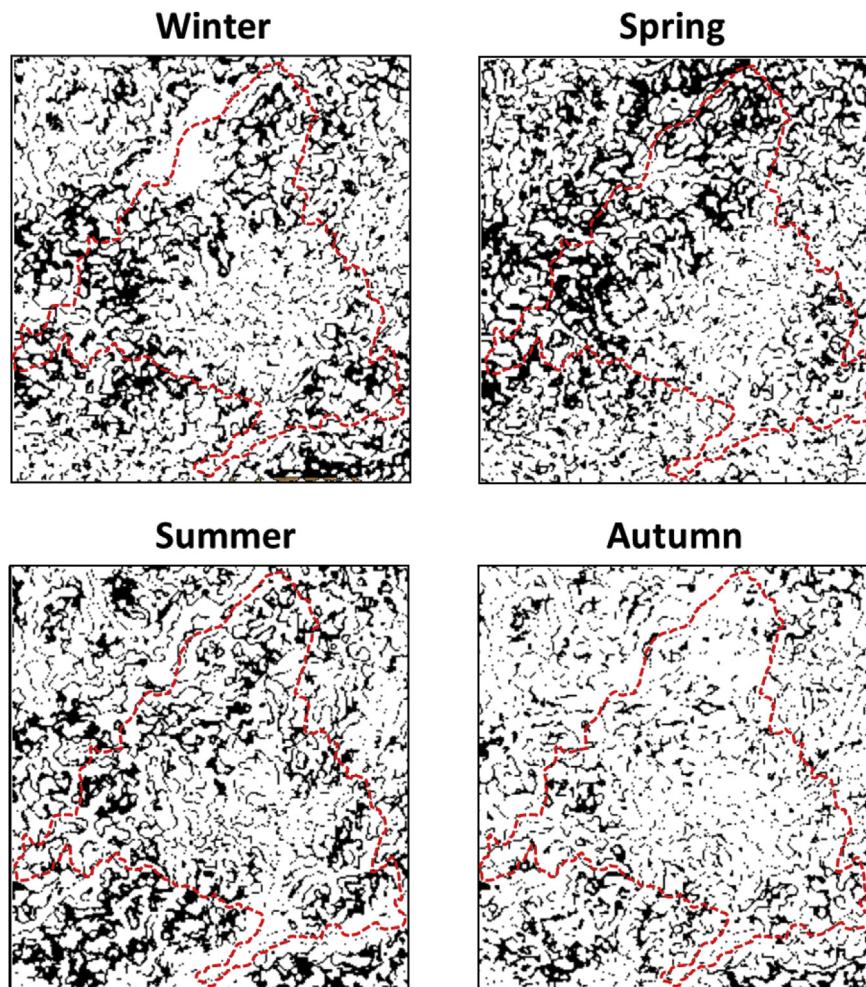

Fig. 9 — Intersection of the two non-singular areas (2005 and 2011) calculated per season. The intersection areas are shown as black pixels. Dashed red lines are the limits of the Autonomous Community of Madrid.

regression lines were based on obtaining $R^2 \geq 0.98$ (Cheng, 1999b).

3.3. Non-singular areas

In Fig. 8 non-singular areas are shown for each analysed date. Black pixels are the points for which $\alpha_{Tmin} \leq \alpha(x) \leq \alpha_{Tmax}$, i.e., the non-singular areas. Therefore, black connected pixels constitute potential areas with normal or log-normal statistical distributions.

In Table 2, the percentage of non-singular areas with respect to the total area is shown for all dates and years. In the dry year (2005), the percentage of non-singular areas in all seasons is quite similar, probably due to the lower climate contrast among seasons. On the other hand, spring is the season with more non-singular areas in the wet year (2011), probably due to the greater climate contrast with the other seasons. Therefore, a majority of normal or log-normal distributions is expected in spring.

The lowest percentage of non-singular areas is always found in autumn, independently of the type (dry or wet) year. This is probably due to the increase of the NDVI spatial variability, indicating that, for several reasons such as topography and rainfall heterogeneity, there are certain areas that achieve a high NDVI value faster than others.

The intersection of non-singular areas per season (intersection area) was obtained by intersecting the two non-singular areas calculated per season (see Fig. 9). Each intersection area was obtained as follows:

- Intersection area (winter) = Non-singular area (17/01/05) & Non-singular area (25/01/11).
- Intersection area (spring) = Non-singular area (23/04/05) & Non-singular area (15/04/11).
- Intersection area (summer) = Non-singular area (20/07/05) & Non-singular area (20/07/11).
- Intersection area (autumn) = Non-singular area (24/10/05) & Non-singular area (24/10/11).

where "&" means "logical and". This intersection area can be interpreted as the area which maintains non-singularity over the two analysed years. The percentage of this intersection area (per season) with respect to the total area is shown in Table 2. This percentage gives us an insight into the spatio-temporal variability of the non-singular areas, since two extreme years were used for the study (wet and dry years). In winter and summer this percentage is very similar (~24%). The highest non-singular intersection area is found in spring (27.2%). Hence, spring is the season with more stability in non-singular areas across years. The lowest intersection area is found in autumn (14.7%), probably due to the high spatial variability in NDVI maps.

Figure 9 shows that the spatial distribution of non-singular intersection areas (black pixels) is extremely dispersed for each season, confirming the multifractal pattern of NDVI maps where different α-sets are very intertwined. This reflects the strong influence that climatic factors, i.e. precipitation and temperature, have in temporal and spatial patterns of NDVI.

At this point it is important to remember that 8 NDVI maps (and so 8 dates) were selected as representative maps of each season in two contrasting years, a dry (2005) and a wet year (2011). Although the results obtained are not statistically significant, in strict sense, the differences found in this study are relevant; pointing out that this methodology could potentially delimit areas that are statistically homogeneous.

4. Conclusions

First, it was proved that the initial assumption of multifractality applied to NDVI maps is reasonably valid in a particular range of scales. Then, it was also proved that the MFS change through the seasons showed a characteristic pattern. It is important to realise that the bandwidth $\Delta\alpha$ has the smallest value during spring, showing the lowest complexity of the scaling structure in the NDVI map. It is also important to note how the symmetry changes from right handed ($\Delta f < 0$) in winter and spring to left handed ($\Delta f > 0$) in summer and autumn. This means that in winter/spring lower NDVI values produce more multifractal complexity than the higher NDVI values. The opposite happens in summer/autumn.

Then, it was shown that spatial analysis of NDVI concentration by using singularity maps can offer similar interpretations to those Cheng applies in detecting anomalous element concentrations within a multifractal framework. Particularly in this study, non-singular areas were calculated in the singularity maps. Singularity map calculation has been a useful tool in establishing NDVI areas where normal or lognormal statistics can be supposed ($\alpha \cong 2$). To find these areas, the C−A method was used to calculate where positive and negative anomalous singularity exponents begin.

It was shown that non-singular areas change through the seasons and different years. It is important to note that the percentage of non-singular areas in the spring depends greatly on the type of year (dry or wet). It takes the highest value of all seasons in a wet year, but it is quite similar to other seasons in a dry year. By contrast, the lowest percentage of non-singular areas was always found in autumn, independent of the (dry or wet) year, probably due to the higher NDVI spatial variability.

The intersection of singularity maps for every season and different years could be the starting point for establishing potential "stable non-singular areas" in time. In this paper it was shown that spring is the season with the highest non-singular intersection area. Hence, in this season the highest amount of area was found which maintained normal or lognormal statistics through the two different years.

In further research, the use of singularity maps to define non-singular areas in the index-based drought insurance context could be explored. An example of drought quantification by NDVI is found in the Spanish insurance. In this kind of insurance, a drought event occurs when the current NDVI is below a NDVI threshold for a specific period of time. This threshold is calculated assuming Gaussian statistics "all over the places". Therefore, using the singularity map analysis, this index-based insurance could take into account the spatio-temporal variability that NDVI maps show. It will also be necessary to increase the number of different dates to improve the statistical significance of the results and to increase the resolution of the analysed images to cover specific vegetation areas.

Summary table	
Parameter	Definition
$A(a_{j,k})$	Matrix of 256 rows $\times$ 256 columns with NDVI values.
$\mu_i = \dfrac{\sum_{j,k\ \in\ i-cell} a_{j,k}}{\sum_{j=1}^{256}\sum_{k=1}^{256} a_{j,k}}$	Measure or normalised probability distribution for the NDVI maps: probability value of the cell i of side r.
$\alpha(x,y) = \lim\limits_{r\to 0} \dfrac{\ln \mu_i}{\ln r}$	Singularity exponents for the NDVI maps which characterise the anomalous spatial behaviour.
$A(\alpha(x,y) \geq c)$	Area constituted by singularity exponents $\alpha(x,y)$ greater than a given value c (C–A model)
$A(\alpha(x,y) < c)$	Area constituted by singularity exponents $\alpha(x,y)$ lower than a given value c (C–A model)
α_{Tmin}	Threshold in the set of positive singularities calculated by the C–A model.
α_{Tmax}	Threshold in the set of negative singularities calculated by the C–A model.
$\Delta\alpha = \alpha_{max} - \alpha_{min}$	Difference of the extreme singularities in the MFS
$\Delta f = f(\alpha_{max}) - f(\alpha_{min})$	Difference of the extreme fractal dimensions in the MFS

Acknowledgements

REFERENCES

Agterberg, F. P. (1995). Power-law versus lognormal models in mineral exploration. In H. S. Mitri (Ed.), *Computer applications in the mineral industry, proceedings of the third Canadian conference on computer applications in the mineral industry* (pp. 17–26).

Alonso, C., Tarquis, A. M., & Benito, R. M. (2005). Multifractal characterization of multispectrum satellite images. *Geophysical Research Abstracts, 7*, 05413.

Alonso, C., Tarquis, A. M., Benito, R. M., & Zúñiga, I. (2007). Scaling properties of vegetation and soil moisture indices: Multifractal and joint multifractal analysis. *Geophysical Research Abstracts, 9*, 11643.

Alonso, C., Tarquis, A. M., Benito, R. M., & Zúñiga, I. (2008). Influence of spatial and radiometric resolution of satellite images in scaling/multiscaling behavior. *Geophysical Research Abstracts, 10*. EGU2008-A-06184.

Alonso, C., Tarquis, A. M., Zúñiga, I., & Benito, R. M. (2017). Spatial and radiometric characterization of multi-spectrum satellite images through multi-fractal analysis. *Nonlinear Processes in Geophysics, 24*, 141–155.

Chantarat, S., Mude, A. G., Barrett, C. B., & Carter, M. R. (2013). Designing index-based livestock insurance for managing asset risk in northern Kenya. *Journal of Risk and Insurance, 80*(1), 205–237.

Cheng, Q. (1999a). Multifractality and spatial statistics. *Computers and Geosciences, 25*, 949–961.

Cheng, Q. (1999b). Spatial and scaling modelling for geochemical anomaly separation. *Journal of Geochemical Exploration, 65*, 175–194.

Cheng, Q. (2001). Singularity analysis for image processing and anomaly enhancement. In *Proceedings IAMG'01, international association for mathematical geology, Cancun, Mexico, 6–12 September*. CD-ROM.

Cheng, Q. (2006). GIS based fractal/multifractal anomaly analysis for modeling and prediction of mineralization and mineral deposits. In J. R. Harris (Ed.), *GIS application in the Earth Sciences – GAC special paper, geological association of Canada special book* (pp. 285–296).

Cheng, Q. (2007). Mapping singularities with stream sediment geochemical data for prediction of undiscovered mineral deposits in Gejiu, Yunnan province, China. *Ore Geology Reviews, 32*, 314–324.

Cheng, Q. (2008). Modeling local scaling properties for multiscale mapping. *Vadose Zone Journal, 7*, 525–532.

Cheng, Q., & Agterberg, F. P. (1996). Multifractal modeling and spatial statistics. *Mathematical Geology, 28*, 1–16.

Cheng, Q., Agterberg, F. P., & Ballantyne, S. B. (1994). The separation of geochemical anomalies from background by fractal methods. *Journal of Geochemical Exploration, 51*, 109–130.

Dalezios, N. R., Blanta, A., Spyropoulos, N. V., & Tarquis, A. M. (2014). Risk identification of agricultural drought for sustainable Agroecosystems. *Natural Hazards and Earth System Sciences, 14*, 2435–2448.

Evertsz, C. J. G., & Mandelbrot, B. B. (1992). Multifractal measures (appendix B). In H. Peitgen, H. Jürgens, & D. Saupe (Eds.), *Chaos and fractal new frontiers of science* (pp. 922–953). New York: Springer-Verlag.

Falconer, K. (2003). *Fractal Geometry. Mathematical foundations and applications* (2nd ed.). West Sussex: John Wiley & Sons.

Feder, J. (1989). *Fractals*. New York: Plenum Press.

Flynn, E. S. (2006). *Using NDVI as a pasture management tool*. Master Thesis. University of Kentucky.

Gouveia, C., Trigo, R. M., & DaCamara, C. C. (2009). Drought and vegetation stress monitoring in Portugal using satellite data. *Natural Hazards and Earth System Sciences, 9*, 185–195.

Halsey, T. C., Jensen, M. H., Kadanoff, L. P., Procaccia, I., & Shraiman, B. I. (1986). Fractal measures and their singularities: The characterization of strange sets. *Physical Review A, 33*, 1141–1151.

Hayes, M. (2004). *Comparison of major drought indices*. National Drought Mitigation Centre. http://drought.unl.edu/Planning/Monitoring/ComparisonofIndicesIntro.aspx.

Journel, A. G., & Huijbregts, Ch. J. (1978). *Mining geostatistics*. San Diego: Academic Press.

Keyantash, J., & Dracup, J. A. (2002). The quantification of drought: An evaluation of drought indices. *Bulletin of the American Meteorological Society, 83*, 1167–1180.

Lavallee, D., Lovejoy, S., Schertzer, D., & Ladoy, P. (1993). Nonlinear variability of landscape topography: Multifractal analysis and simulation. In L. De Cola, & N. Lam (Eds.), *Fractals in geography* (pp. 158–192). Englewood Cliffs, New Jersey: PTR, Prentice Hall.

Liu, Y., Xia, Q., Cheng, Q., & Wang, X. (2013). Application of singularity theory and logistic regression model for tungsten polymetallic potential mapping. *Nonlinear Processes in Geophysics, 20*, 445–453.

Lovejoy, S., Tarquis, A. M., Gaonac'h, H., & Schertzer, D. (2008). Single and Multiscale remote sensing techniques,

multifractals and MODIS derived vegetation and soil moisture. *Vadose Zone Journal, 7*(2), 533—546.

LP DAAC (Land Processes Distributed Active Archive Center): Surface reflectance 8-day L3 Global 500m. (2014). NASA and USGS. https://lpdaac.usgs.gov/products/modis_products_table/mod09a1.

Makaudze, E. M., & Miranda, M. J. (2010). Catastrophic drought insurance based on the remotely sensed normalised difference vegetation index for smallholder farmers in Zimbabwe. *Agrekon, 49*(4), 418—432.

Peebles, P. Z. (1987). *Probability, random variables and random signal principles* (2nd ed.). Singapore: McGraw-Hill.

Poveda, G., & Salazar, L. F. (2004). Annual and interannual (ENSO) variability of spatial scaling properties of a vegetation index (NDVI) in Amazonia. *Remote Sensing of Environment, 93*, 391—401.

Saravia, L. A., Giorgi, A., & Momo, F. (2012). Multifractal spatial patterns and diversity in an ecological succession. *PLoS One, 7*(3). http://dx.doi.org/10.1371/journal.pone.0034096.

Schertzer, D., & Lovejoy, S. (1987). Physical modeling and analysis of rain and clouds by anisotropic scaling of multiplicative processes. *Journal of Geophysical Research: Atmospheres, 92*, 9693—9714.

Schertzer, D., & Lovejoy, S. (Eds.). (1991). *Nonlinear variability in geophysics* (p. 318). Dordrecht, The Netherlands: Kluwer Academic Publishers.

Scheuring, I., & Riedi, R. H. (1994). Application of multifractals to the analysis of vegetation pattern. *Journal of Vegetation Science, 5*, 489—496.

Sepulcre-Canto, G., Horion, S., Singleton, A., Carrao, H., & Vogt, J. (2012). Development of a combined drought indicator to detect agricultural drought in Europe. *Natural Hazards and Earth System Sciences, 12*, 3519—3531.

Solé, R. V., & Bascompte, J. (2006). *Self-organization in complex ecosystems*. Princeton University Press.

Sornette, D. (2004). *Critical phenomena in natural sciences: Chaos, fractals, self-organization, and disorder* (2nd ed.). New York: Springer.

Sotelo Pérez, M. (2013). Las infraestructuras históricas, nuevos paisajes culturales del agua. *Territorio y medio ambiente en la Comunidad de Madrid, 14*(1), 87—115.

Tarquis, A. M., Losada, J. C., Benito, R., & Borondo, F. (2001). Multifractal analysis of the tori destruction in a molecular Hamiltonian system. *Physical Review E, 65*(9), 0126213.

Turcotte, D. L. (1997). *Fractals and chaos in geology and geophysics* (2nd ed.). Cambridge, UK: Cambridge Univ. Press.

Veneziano, D. (2002). Multifractality of rainfall and scaling of intensity—duration—frequency curves. *Water Resources Research, 38*, 1—12.

Xie, S., Cheng, Q., Chen, G., Chen, Z., & Bao, Z. (2007). Application of local singularity in prospecting potential oil/gas targets. *Nonlinear Processes in Geophysics, 14*, 285—292.